



Ni₂P/Beta@SBA-16 core-shell catalyst with tunable shell thickness for the hydrodenitrogenation of quinoline

Hanzhang Gong, Yuan Zhuang, Xiao Zhang^{*}, Jian Liu^{*}, Shuyuan Li

State Key Laboratory of Heavy Oil Processing, College of Science, China University of Petroleum, Beijing 102249, China

ARTICLE INFO

Keywords:

Ni₂P catalyst
Hydrodenitrogenation
Quinoline
Multistage porous zeolite
Core-shell

ABSTRACT

A series of core-shell structural hydrodenitrogenation (HDN) catalyst supports, using H-Beta zeolite nanoparticles as the core and tunable mesoporous materials SBA-16 thin film thickness as shell, were designed and controllably synthesized. The corresponding Ni₂P catalyst were prepared, and their catalytic performances were tested for quinoline HDN. It was found that the high external surface area provided by the mesoporous shell layer of the core-shell catalyst favored the formation of Ni₂P nanoparticles with more uniform particle size. The Py-IR result indicates that the SBA-16 shell thickness plays an important role in influencing the ratio of the amount of Bronsted and Lewis acid sites on the catalyst. The H₂-TPR results indicates that the introduction of core-shell structure can adjust the metal-support interactions (MSI) of materials. The core-shell support with suitable shell thickness (70 nm) exhibits a wide pore structure, large surface area and sufficient amounts of Lewis and Bronsted acid sites. These properties contribute to the formation of tiny and size homogeneous (4.6 nm) Ni₂P nanoparticles. Smaller Ni₂P particles present more active sites, which increases catalytic activity. The Ni₂P/H-Beta@SBA-16-2 catalyst with the most suitable shell thickness exhibited a higher reaction rate constant and TOF for HDN reaction of quinoline.

1. Introduction

Hydrogenation refinement remains an effective method for large-scale production of low sulfur nitrogen crude oil [1]. Since the S content is higher than the N content in crude oil, hydrogenation research mainly focuses on hydrodesulfurization (HDS) [2]. However, environmental regulations in many countries have become increasingly stringent, prompting lower nitrogen-containing standards for fuel oils. Also, competitive adsorption on active sites caused by the presence of nitrogenous compounds hinders the removal of sulfur-containing compounds [3–6]. Therefore, the development of highly active HDN catalysts is an important approach towards achieving high-quality clean crude oil production.

Currently, conventional HDN catalysts are γ -Al₂O₃ supported metal sulfide (CoMo or NiMo) catalysts [7–10], which have low hydrogenation activity and cannot achieve significant removal of nitrogenous compounds under mild conditions [11]. Noble metal catalysts such as Pd, Pt, and Pd-Pt exhibit high hydrogenation activity [12–14]. However, noble metal catalysts have limited applications due to their cost, sensitivity to sulfur and ease of toxic deactivation [15]. In recent years, metal

phosphides such as (CoP, MoP, and Ni₂P) have attracted much attention as novel hydrogenation catalysts [16–20]. In particular, nickel phosphide catalysts which approximate the prismatic structure of the sphere type, exhibit a higher density of coordinatively unsaturated surface atoms, and thus better catalytic activity than the layered structure between the crystal lattices of conventional sulfide catalysts [21]. It is well known that the catalytic performance of Ni₂P catalyst is closely related to its morphology. The Ni₂P particles possess two types of Ni sites, Ni (1) site is tetrahedral surrounded by four neighboring P atoms whereas Ni (2) site is square pyramidal surrounded by five neighboring P atoms. The former is the active center for direct denitrification because the lower coordination number Ni (1) site is more easily take on a nitrogen atom. While smaller Ni₂P nanoparticles contain more active centers for Ni (2), essential for hydrogenation [22,23]. Therefore, increasing the dispersion of Ni₂P active phase can effectively increase the number of active sites in the hydrogenation center, thereby improving the hydrogenation performance of the catalyst. However, the bulk Ni₂P catalyst has a small surface area and easily sinters during the reduction process, resulting in low catalyst dispersion and thus a relatively low HDN activity [24].

Compared with the bulk catalyst, the supported catalyst has the

^{*} Corresponding authors.

E-mail addresses: zhangxiao@cup.edu.cn (X. Zhang), liujian@cup.edu.cn (J. Liu).

<https://doi.org/10.1016/j.apcatb.2023.122574>

Received 12 November 2022; Received in revised form 27 February 2023; Accepted 3 March 2023

Available online 9 March 2023

0926-3373/© 2023 Published by Elsevier B.V.

advantages of high specific surface area and more surface active centers [25,26]. In addition, the framework of the hydrogenation catalyst supports the active metal and allows it to disperse homogeneously while providing sufficient space for the hydrogenation reaction [27]. Currently, Ni_2P catalysts with porous silicon oxide as support have received much attention [28–32]. It has been reported that Ni_2P catalysts supported on mesoporous silica materials can increase the dispersity of the active phase of metal phosphines due to the large surface area of silica [32,33]. However, the Ni_2P precursor formed using neutral materials as support showed weak interaction with the support surface, while the strong interaction of Ni species with the support surface could reduce the aggregation of Ni_2P particles during reduction and calcination, thus further improving the activity of catalysts [34].

The conventional microporous aluminosilicates zeolite, which have excellent properties such as high specific surface area, tunable pore size, strong surface acidity, and negatively charged frameworks, have become a focus of research efforts in the field of hydrogenation [35,36]. Zhang et al. reported a series of Ni_2P catalysts supported on nano sheet mordenite (NS-HMOR). The high surface area of NS-HMOR and abundant acidic hydroxyl groups, favor the formation of highly dispersed Ni_2P particles. These highly dispersed, small Ni_2P particles enable the catalyst to have high hydrodesulfurization activity and stability [37]. The high specific surface area of zeolites facilitates the dispersion of metal catalysts, and the surface acidity and framework electronegativity of zeolites result in strong interactions with the supported metals [38]. Moreover, the micropores of the zeolite framework enable the formed nanoscale metal particles to be anchored inside the microporous pore channels [39,40]. These properties can prevent the accumulation and sintering of Ni_2P during calcination and reduction.

Although the catalysts supported on microporous zeolites show better catalytic performance in HDN reaction, some aromatic hydrocarbons have large kinetic dimensions, and the reactant molecules cannot diffuse into the microporous channels [38,41,42]. In addition, the excessive acidic sites of some aluminosilicate zeolites may cause hydrolytic cleavage during hydrogenation reactions, leading to carbon accumulation and focusing, resulting in catalyst deactivation [43,44]. To solve these problems, researchers have developed zeolites with multistage pores [45–47]. Huo et al. reported a novel microporous mesoporous composite molecular sieve (denoted as LMC) using nanocrystalline clusters of zeolite L as precursor. Characterization of the LMC indicated that the surface area, pore volume, and pore size were significantly increased compared with conventional microporous zeolite L, and that the LMC had an appropriate amount of acid and acid distribution. Therefore, LMC exhibited higher hydrogenation activities than catalysts with microporous zeolite L, mesoporous Al-MCM-41, and conventional alumina as supports [42].

In the present work, we have synthesized novel HDN catalysts supported on porous zeolites with a core-shell structure. Specifically, a series of core-shell materials with different shell thicknesses containing mesoporous material SBA-16 as shell layer and H-Beta zeolite as core were prepared by liquid phase deposition. Furthermore, smaller Ni_2P nanoparticles were grown in the core-shell material using the hypophosphate disproportionation method to form highly efficient HDN reaction catalysts.

2. Experimental

2.1. Preparation of supports

2.1.1. Preparation of H-beta zeolite and SBA-16 materials

Tetraethylammonium hydroxide (TEAOH) was used as a template for the synthesis of β Zeolites. The specific steps were as follows: 0.24 g NaOH was added to a mixed solution of 34.92 g TEAOH and 40 g silica sol, well dissolved with stirring, 42.48 g deionized water and 0.82 g aluminum isopropoxide were added to the above solution and kept stirring for 24 h. Subsequently, the above solution was transferred into a

Teflon hydrothermal autoclave to react at 140 °C for 96 h. The obtained samples were filtered, washed to neutrality, oven dried at 60 °C for 12 h, and subjected to programmed calcination at 550 °C for 6 h. After the product is cooled, Na-beta zeolites were obtained by grinding. In addition, NH_4Cl solution was added to the above Na-beta samples for ion exchange and H-beta zeolites were subsequently obtained after filtration, washing, drying and calcination.

The specific procedure for the synthesis of SBA-16 materials using triblock copolymer F127 ($\text{EO}_{106}\text{PO}_{70}\text{EO}_{106}$) as a template is as follows: 3 g F127, 13.9 mL concentrated hydrochloric acid and 144 mL deionized water were mixed well by stirring, followed by dropwise addition of 11 mL n-butanol as well as 15.3 mL tetraethyl silicate (TEOS). The above solution was transferred into a Teflon hydrothermal autoclave and heated at 100 °C for 24 h. The SBA-16 sample was obtained after subsequent filtration washing, drying at 60 °C for 12 h, and calcination at 550 °C for 6 h.

2.1.2. Preparation of H-beta@SBA-16-x core-shell composite materials

The composite materials were synthesized using a liquid-phase deposition method. The thickness of the shell layer was controlled by varying the ratio of TEOS and zeolites. Typically, 0.193 g F127 was added into 20 mL 1 M HCl and stirred at room temperature for 2 h to fully dissolve it. To the above solution 716.5 μL n-butanol was added. After it was mixed uniformly, 0.5 g H-Beta zeolite was added. A certain amount of TEOS was slowly added dropwise into this liquid mixture after stirring for 2 h, followed by ultrasonication for 2 h and stirring for 24 h so that TEOS and H-Beta were completely dispersed in the solution. The above solution was subsequently transferred into a hydrothermal autoclave and reacted at 100 °C for 48 h. The resulting samples were filtered, washed to neutrality, dried at 60 °C for 12 h, and calcined at 550 °C for 6 h. After being cooled to room temperature and grinding, a series of composites were obtained. The composite materials with different amounts of TEOS (with the mass ratios of TEOS/H-Beta = 1, 2, and 4) are denoted as H-beta@SBA-16-x (x = 1, 2, and 3).

2.2. Preparation of supported Ni_2P catalysts

The supports were treated by an equal volume immersion method, with nickel chloride as the nickel source, for 12 h and oven dried at 110 °C for 2 h. Sodium hypophosphite (NaH_2PO_2) and the above precursor at a certain phosphorus nickel ratio were placed in two quartz boats, respectively. The quartz boats were placed sequentially in a tubular furnace, with the NaH_2PO_2 quartz boat in front and the precursor quartz boat behind along the direction of nitrogen flow. Then calcined at 300 °C for 2 h, at a rate of 2 °C·min⁻¹ in a flow of N_2 (10 mL·min⁻¹). The Ni loading in the catalyst was 10.0 wt%. The catalysts on the different supports were denoted as $\text{Ni}_2\text{P}/\text{H-beta}$, $\text{Ni}_2\text{P}/\text{SBA-16}$ and $\text{Ni}_2\text{P}/\text{H-beta@SBA-16-x}$ (x = 1, 2, and 3).

2.3. Characterization and catalytic evaluation

The analytical methods of X-ray diffraction (XRD), nitrogen adsorption-desorption, scanning electron microscopy (SEM), transmission electron microscopy (HRTEM), Fourier transform infrared spectroscopy (FT-IR), FT-IR of the adsorbed pyridine (Py-FTIR), X-ray photoelectron spectroscopy (XPS), CO chemisorption, H_2 -temperature-programmed reduction (H_2 -TPR) and the catalytic performance evaluation methods are presented in the [Supporting Information](#). Furthermore, the calculation methods of k_{HDN} and TOF of HDN reaction are also detailed in the [Supporting Information](#).

3. Results

3.1. Support characterization

Wide-angle XRD patterns of the H-beta zeolites, pure SBA-16, as well

as the H-beta@SBA-16-x series of materials are shown in Fig. 1A. From Fig. 1A, only the SBA-16 material exhibits diffraction peaks at around 24° ascribed to amorphous SiO_2 . The H-beta zeolites exhibited several diffraction peaks at $5\text{--}10^\circ$ and $20\text{--}25^\circ$ assigned to BEA zeolite structure and characteristic of a high degree of crystallinity. The H-beta@SBA-16 composite materials show the same diffraction peaks at the same positions, indicating that the introduction of SBA-16 shell layer does not destroy the BEA structure of the zeolites. Meanwhile, the intensity of the corresponding diffraction peaks appeared to decay due to the material surface coated SBA-16 shell layer, and the intensity of the diffraction peaks weakened with increasing shell thickness.

Small angle XRD diffraction results of these materials are shown in Fig. 1B. The SBA-16 material shows a sharp diffraction peak at 1° , corresponding to the (110) crystal plane diffraction peak of SBA-16 material. This observation indicates that the material has a long-range ordered mesoporous structure. In contrast, no obvious diffraction peaks appeared for the H-Beta zeolite, indicating the absence of any ordered mesoporous structure in the original H-Beta zeolite. The composites (H-beta@SBA-16-2 and H-beta@SBA-16-3) give rise to broader diffraction peaks and a shift to lower angles, which indicates that the material unit cell parameters become larger, corresponding to a larger periodic interplanar spacing. In addition, small angle XRD characterization was performed after mechanically mixing H-Beta and SBA-16 (Fig. S1 of the Supplementary Information). From Fig. S1, a single identical and weaker diffraction peak appeared for the mechanically blended sample. Therefore, the characteristic peaks presented, in both the small and wide angle XRD ranges, indicate that the synthesized composites possess both microporous H-Beta zeolite and ordered mesoporous structures.

The nitrogen adsorption-desorption results for the samples are

shown in Fig. 1C and D. As can be seen in Fig. 1C, the pure H-Beta zeolite exhibited a typical type I adsorption isotherm. In contrast, pure mesoporous SBA-16 shows typical composites with type IV adsorption isotherms and H2 type hysteresis loops. This suggests that the H-beta is a microporous material, while the SBA-16 is a highly ordered mesoporous material. It can also be seen from the mesoporous pore size distribution curve (Fig. 1D) that the SBA-16 material exhibits a sharp distribution peak at 4 nm. The composites exhibited type I and type IV mixed adsorption isotherms. As the ratio of silicon source to zeolites increased, a saturated adsorption plateau appeared on the composite isotherms, reflecting the formation of mesopores with a more uniform pore size distribution. The pore size distribution curves show that the core-shell materials have a wider distribution of mesopores ranging from 5 to 15 nm in addition to the peak centered at 4 nm. The latter was attributed to the deposition of silicon sources on the interface of the zeolite core that generates a large number of irregular wormlike mesopores while the shell continued to grow under the guidance of the F127 template and generated ordered mesoporous pores. The pore structure parameters of the supports are summarized in Table 1. With the introduction of a mesoporous shell layer, the microporous pore volume of the composites decreases, while the surface area and pore volume increase. The external surface area increases with increasing shell thickness.

The micro morphology and mesostructure of the materials were analyzed by SEM and TEM. It is clear from the SEM results that the pure H-Beta sample consists of many agglomerations of similar sized grains (Fig. 2 a1). The SBA-16 exhibits a typical amorphous silica structure (Fig. 2 e1). The composites retained the basic shape of the beta zeolite crystals, the external surface of which was successfully coated by a layer of amorphous SBA-16 shells, and the crystallinity of the supported

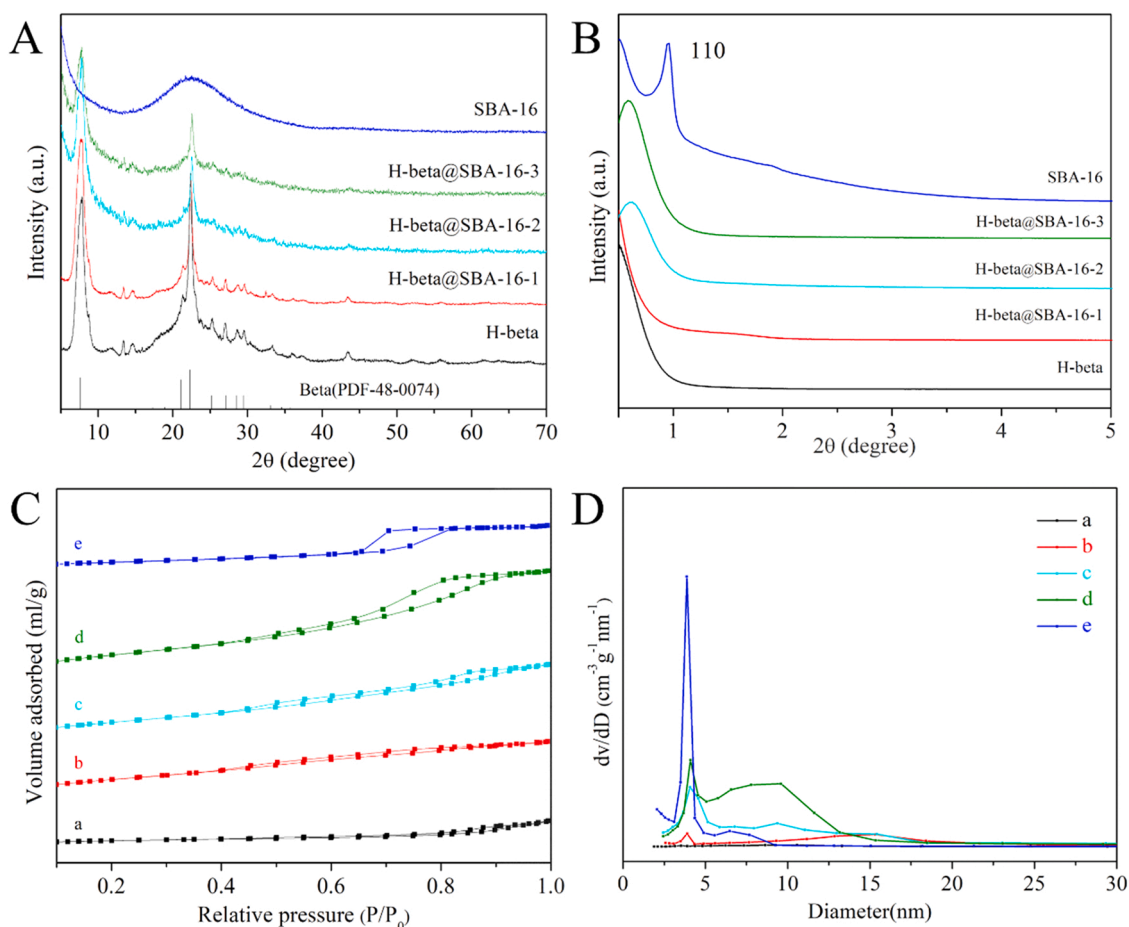


Fig. 1. Wide angle XRD patterns of the prepared supports (A), small angle XRD patterns of the prepared supports (B), N_2 adsorption-desorption patterns (C) and pore size distributions (D) of series supports: H-beta (a), H-beta@SBA-16-1 (b), H-beta@SBA-16-2 (c), H-beta@SBA-16-3 (d), SBA-16 (e).

Table 1
Textural properties of the materials.

Sample	S_{BET}^a (m^2g^{-1})	S_{ext}^b (m^2g^{-1})	S_{mic}^c (m^2g^{-1})	V_{meso}^c (cm^3g^{-1})	V_{micro}^c (cm^3g^{-1})	Si: Al ^d
H-beta	477.3	107.2	370.1	0.17	0.18	25.5
H-beta@SBA-16-1	522.3	216.7	305.6	0.44	0.08	26.3
H-beta@SBA-16-2	595.9	366.3	229.6	0.57	0.07	29.9
H-beta@SBA-16-3	634.8	437.9	196.9	0.79	0.03	57.6
SBA-16	798.1	665.5	132.6	0.81	0.01	-

^a Obtained by the BET method.

^b External surface area obtained by the t-plot method.

^c Obtained by the t-plot method.

^d Given by ICP analysis.

particles gradually weakened with increasing shell thickness. From the TEM image and its enlargement, it can be seen that the pure H-Beta sample is characterized by a grain of about 500 nm with a smooth external surface. The SBA-16 is a typical ordered mesoporous material with a pore size of approximately 5 nm. In contrast, the composites exhibited an obvious bilayer structure with a core of H-Beta zeolite. The SBA-16 shell layer was uniformly coated on the external surface of H-Beta zeolite, and its shell thickness was approximately 20 nm, 70 nm, 280 nm, respectively (Fig. 2 b3, c3 and d3). It is important to note that the shell thickness of the H-Beta@SBA-16-3 is not completely homogeneous and 280 nm is the average calculated after statistics (Fig. S7). In addition, a selected area electron diffraction (SAED) spectrum further proved the formation of a core-shell structure (Fig. 2 c3). According to the SAED results, it can be seen that the core of the composite is crystalline distinguished from the amorphous structure of the shell. In addition, two other core-shell materials were prepared without hydrothermal crystallization, and their TEM images are shown in Fig. S2. As can be seen from the figure, the silicon source grows irregularly on the surface of zeolites through electrostatic adsorption, and its pore channels are disordered worm like mesoporous structures.

The presence of Lewis (L) acid sites can be proven by the appearance of characteristic peaks at 1450 cm^{-1} , 1570 cm^{-1} , and 1610 cm^{-1} in the wavenumber of Py-FTIR. The appearance of characteristic peaks at 1540 cm^{-1} can be assigned to Brönsted (B) acid sites. Moreover, the peak at 1490 cm^{-1} corresponds to both L and B acids.[48] Pyridine adsorbed on the catalyst was degassed at $200\text{ }^{\circ}\text{C}$ and $350\text{ }^{\circ}\text{C}$, respectively. The results at $200\text{ }^{\circ}\text{C}$ represent the total acid amount of the catalyst while those at $350\text{ }^{\circ}\text{C}$ represent the medium strong acid amount. The amount of acid for this series of materials is shown in Fig. 3 and table S1. As can be seen from Fig. 3, H-Beta zeolites exhibited strong absorption peaks at both B and L acid sites, indicating the existence of two kinds of acidic centers in the sample. SBA-16 showed only an absorption peak at the L acid site. While the as synthesized layered composites exhibited weaker absorption peaks for both B and L acid sites, the intensity of the absorption peak was in between that of the two mentioned above. Therefore, the introduction of a mesoporous silica shell layer into microporous zeolites is an effective way to tune the acidic properties of materials. While it is generally believed that the B acid site has a promoting effect on the hydrogenolysis reaction and favors the breakage of C–n bonds in nitrogenous compounds [49–51]. Therefore, the B acid site (provided by H-beta core) on the core-shell support is beneficial to improve the hydrogenation reaction performance.

Infrared characterization can provide more information on the composition and structure of the support material, the occurrence of peaks at different wavenumber positions reacting to the species and vibration of different species within the sample. As shown in Fig. 4, the

sharp peak at 460 cm^{-1} corresponds to the bending vibration of Si–O–Si bond. Meanwhile, all the samples presented weaker absorption peaks at 800 cm^{-1} and 962 cm^{-1} , which were assigned to the symmetric stretching vibration of Si–O–Si bonding and vibration of the Si–OH bond, respectively. In addition, there were two absorption peaks at 520 and 570 cm^{-1} for pure beta zeolites and composites, which were assigned to the double ring vibration absorption peaks of six and five membered rings in the framework structure of BEA zeolites. This illustrates that the composites still retain a basic beta zeolite framework Table 2.

3.2. Catalyst characterization

The XRD patterns of the series catalysts are presented in Fig. 5. All the catalysts show three main peaks at 40.6° , 44.5° , and 47.1° , corresponding to the characteristic peaks of hexagonal Ni_2P (PDF: 03–0953). There are no characteristic diffraction peaks for other phases of Ni or P. The crystal sizes (d_{XRD}) calculated by Scherrer's equation are shown in Table 3. The crystal sizes of $\text{Ni}_2\text{P}/\text{H-beta}$, $\text{Ni}_2\text{P}/\text{H-beta@SBA-16-x}$ ($x = 1, 2$ and 3) and $\text{Ni}_2\text{P}/\text{SBA-16}$ were 12.3 nm , 11.5 nm , 3.9 nm , 5.5 nm and 11.9 nm respectively, indicating that the Ni_2P particles on the core-shell structures catalysts exhibited smaller crystal sizes.

The surface properties of H-beta@SBA-16-2 and SBA-16 by IR spectroscopy and the results are presented in Fig. 6. There were two types of hydroxyl groups present on the surface of H-beta@SBA-16-2, silicon hydroxyl (Si–OH, 3740 cm^{-1}) and acidic framework aluminum hydroxyl (Si–OH–Al, 3610 cm^{-1}). Only silicon hydroxyl groups (Si–OH, 3740 cm^{-1}) were contained on the surface of SBA-16. Upon increasing the metal loading, the absorption intensity of $\text{Ni}_2\text{P}/\text{H-beta@SBA-16-2}$ and $\text{Ni}_2\text{P}/\text{SBA-16}$ bands at 3740 cm^{-1} and 3610 cm^{-1} decreased gradually. For the erosion of 3740 cm^{-1} band should be the interaction that occurs for cationic Ni with silicon hydroxyl groups. While the erosion of 3610 cm^{-1} band indicates that Ni ions has substituted protons on the internal bridged Si–OH–Al sites. This could also indicate the Ni cations to be located in internal Si–ONi–Al bridged positions [52,53]. And the new IR absorption band appeared at 3652 cm^{-1} was assigned to Ni–OH surface groups [54]. It is worth noting that SBA-16 is an amorphous neutral porous material and Ni species undergo weaker interactions with silicon hydroxyl groups. However, the substitution of Ni ions with acidic hydroxyl groups on the surface of H-beta@SBA-16-2 can anchor Ni species and favor the formation of highly dispersed small-sized Ni_2P phase on the surface during calcination and reduction of the catalyst.

The catalyst after loading nickel phosphide was analyzed by TEM. As shown in Fig. 7, Ni_2P particles were loaded on the support as round or oval particles. The Ni_2P nanoparticle sizes of core-shell catalyst were significantly smaller than that of pure zeolite support and mesoporous catalysts. Moreover, as can be seen from the Ni_2P particle size statistics on different catalysts, when pure zeolites were used as the support, the standard deviation of the results of the particle size statistics was larger, which indicates that its nickel phosphide particle size distribution was wider. However, the standard deviation of the results of the particle size statistics for the core-shell catalysts was significantly smaller, and their Ni_2P particle size distributions had a narrower range ($2\text{--}8\text{ nm}$), indicating the formation of more uniform small particle Ni_2P phases on the core-shell catalysts. Moreover, although mesoporous SBA-16 has a high surface area, its average particle size is still larger than that of core shell materials. This is mainly because the introduction of core-shell structure modulated the B and L acid site ratio of the support, increasing the B acid amount. Ni^{2+} species on the catalysts more easily interact strongly (grafting and substitution) with the acidic hydroxyl groups on the material, contributing to the formation of highly dispersed Ni_2P active phases during calcination and reduction. Therefore, the core-shell catalysts with higher B acid content as well as external surface area had the smallest Ni_2P particle size, consistent with the XRD analysis. HRTEM images further demonstrate the formation of Ni_2P phase with its lattice fringes clearly observed in Fig. 7c1 with an interplanar spacing of 0.22 nm and 0.19 nm , corresponding to the (111) and (210) Ni_2P

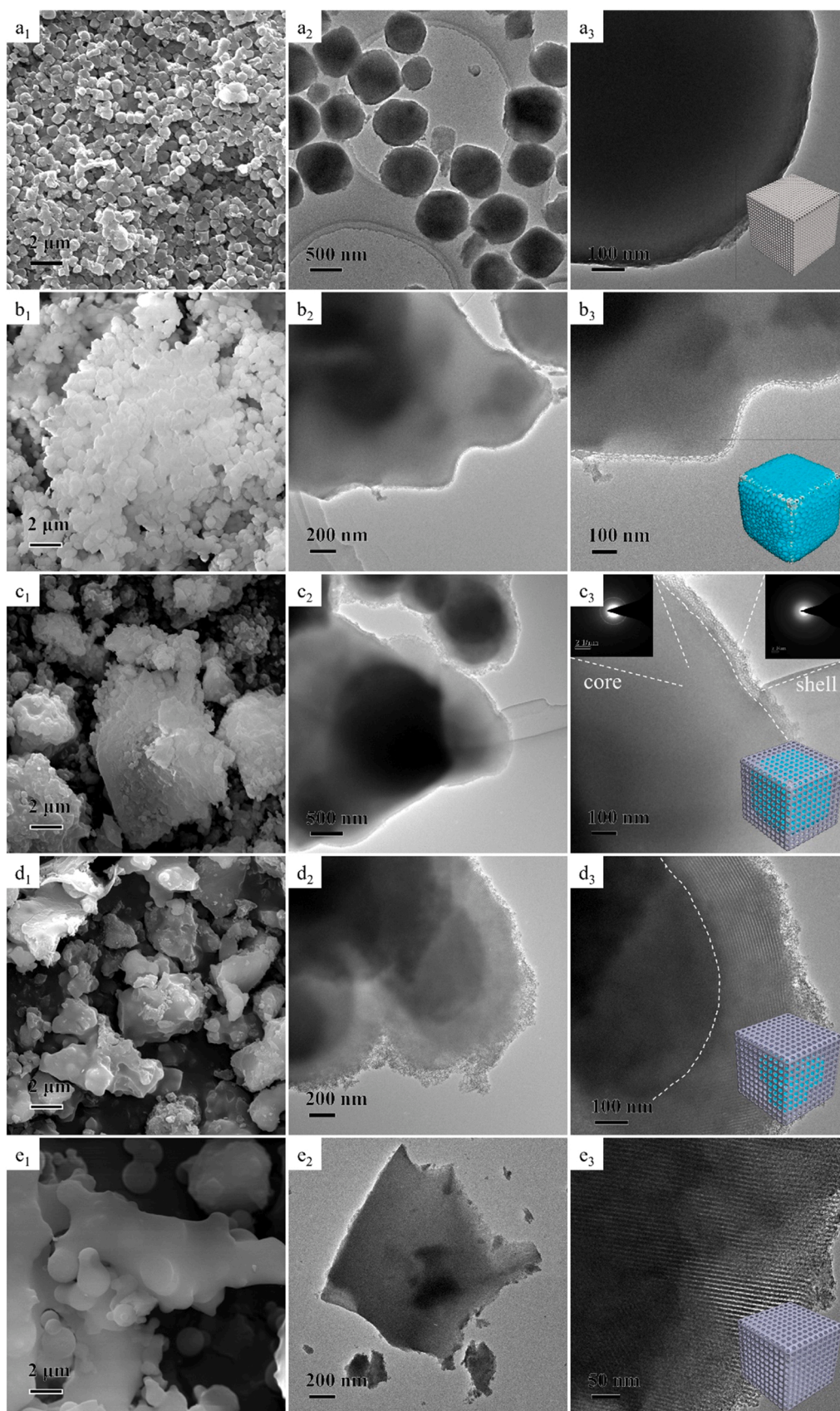


Fig. 2. SEM and TEM images of H-beta (a₁, a₂ and a₃), H-beta@SBA-16-1 (b₁, b₂ and b₃), H-beta@SBA-16-2 (c₁, c₂ and c₃), H-beta@SBA-16-3 (d₁, d₂ and d₃) and SBA-16 (e₁, e₂ and e₃).

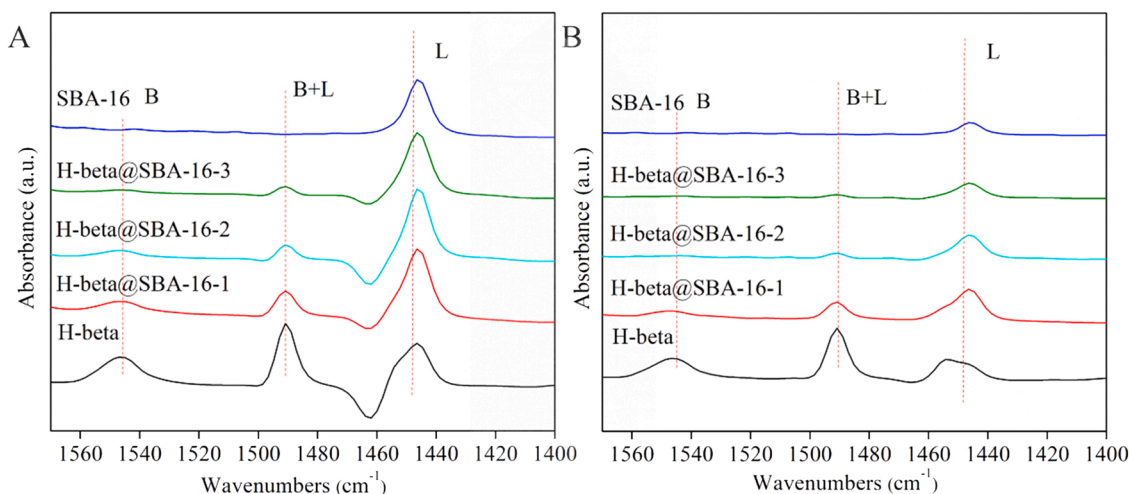


Fig. 3. FT-IR spectra of pyridine adsorbed on supports following desorption at 200 °C (A) and 350 °C (B).

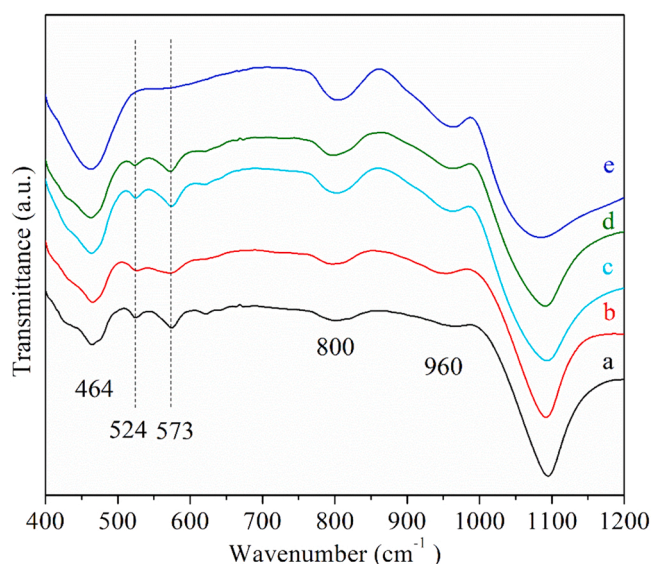


Fig. 4. FT-IR spectra of the prepared supports: H-beta (a), H-beta@SBA-16-1 (b), H-beta@SBA-16-2 (c), H-beta@SBA-16-3 (d), SBA-16 (e).

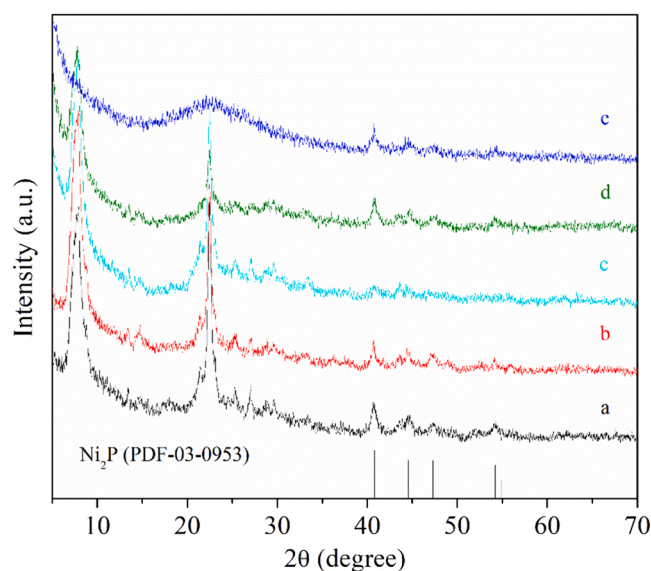


Fig. 5. XRD patterns of series catalysts: Ni₂P/H-beta (a), Ni₂P/H-beta@SBA-16-1 (b), Ni₂P/H-beta@SBA-16-2 (c), Ni₂P/H-beta@SBA-16-3 (d), Ni₂P/SBA-16 (e).

Table 2

The XPS analysis results of the catalyst samples.

Catalysts	Ni2p _{3/2} (binding energy)		P2p _{3/2} (binding energy)		Superficial atomic ratio	
	Ni ²⁺	Ni ₂ P	PO ₃ ⁴⁻	Ni ₂ P	P/Ni	Ni/Si+Al
Ni ₂ P/H-beta	857.2	853.3	134.4	129.6	2.75	0.023
Ni ₂ P/H-beta@SBA-16-2	856.9	853.3	134.2	129.6	2.25	0.025
Ni ₂ P/SBA-16	857.2	853.3	134.5	129.5	2.86	0.013

crystallographic planes, respectively.

The amount of CO chemisorption on the material surface can reflect the dispersion of Ni₂P active phase in the catalyst. Table 3 presents the CO chemisorption results for the different catalysts prepared. As shown in Table 3, the amount of CO chemisorption by the catalysts is Ni₂P/H-beta@SBA-16-2 (96.5 μmolg⁻¹) > Ni₂P/H-beta@SBA-16-3 (65.6 μmolg⁻¹) > Ni₂P/H-beta@SBA-16-1 (63.7 μmolg⁻¹) > Ni₂P/H-beta (50.1 μmolg⁻¹) > Ni₂P/SBA-16 (38.1 μmolg⁻¹), respectively. From these

Table 3

The results of Ni₂P particle size and CO uptake of the catalysts.

Catalysts	D _{xrd} ^a (nm)	D _c ^b (nm)	CO uptake (μmol/g)
Ni ₂ P/H-beta	12.3	11.0	50.1
Ni ₂ P/H-beta@SBA-16-1	11.5	8.9	63.7
Ni ₂ P/H-beta@SBA-16-2	3.9	4.6	96.5
Ni ₂ P/H-beta@SBA-16-3	5.5	11.7	65.6
Ni ₂ P/SBA-16	11.9	18.4	38.1

^a Calculated by Scherrer equation, $D_{xrd} = K\lambda / \beta \cos(\theta)$.

^b Obtained by statistical analyses of the TEM images.

results, the core-shell catalyst exhibited the highest CO adsorption amount, illustrating the high dispersion of the Ni₂P active phase on the support consistent with TEM results.

In order to obtain more information about the valence states and atomic ratios of the catalyst surface species, the catalyst samples after supported Ni₂P phase were analyzed by XPS. The results are shown in Fig. 8 and Table 2. According to the literature, the 2p electron orbitals of Ni atoms decompose into Ni 2p_{3/2} and Ni 2p_{1/2}, and there is one

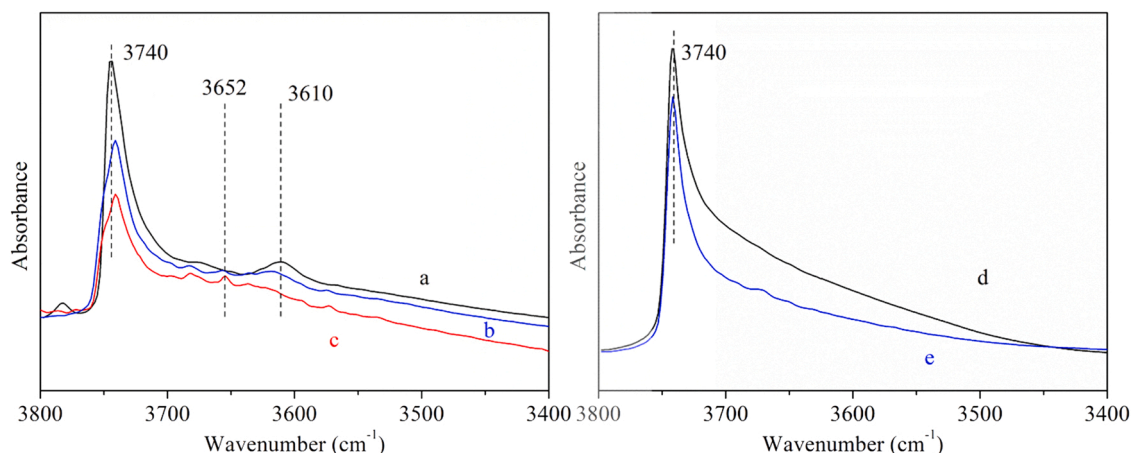


Fig. 6. In-situ IR spectra of the H-beta@SBA-16-2 (a), 2% Ni₂P/H-beta@SBA-16-2 (b), 5%Ni₂P/H-beta@SBA-16-2 (c), SBA-16 (d) and 2%Ni₂P/SBA-16 (e). The spectra were recorded at room temperature after the sample was outgassed at 400 °C.

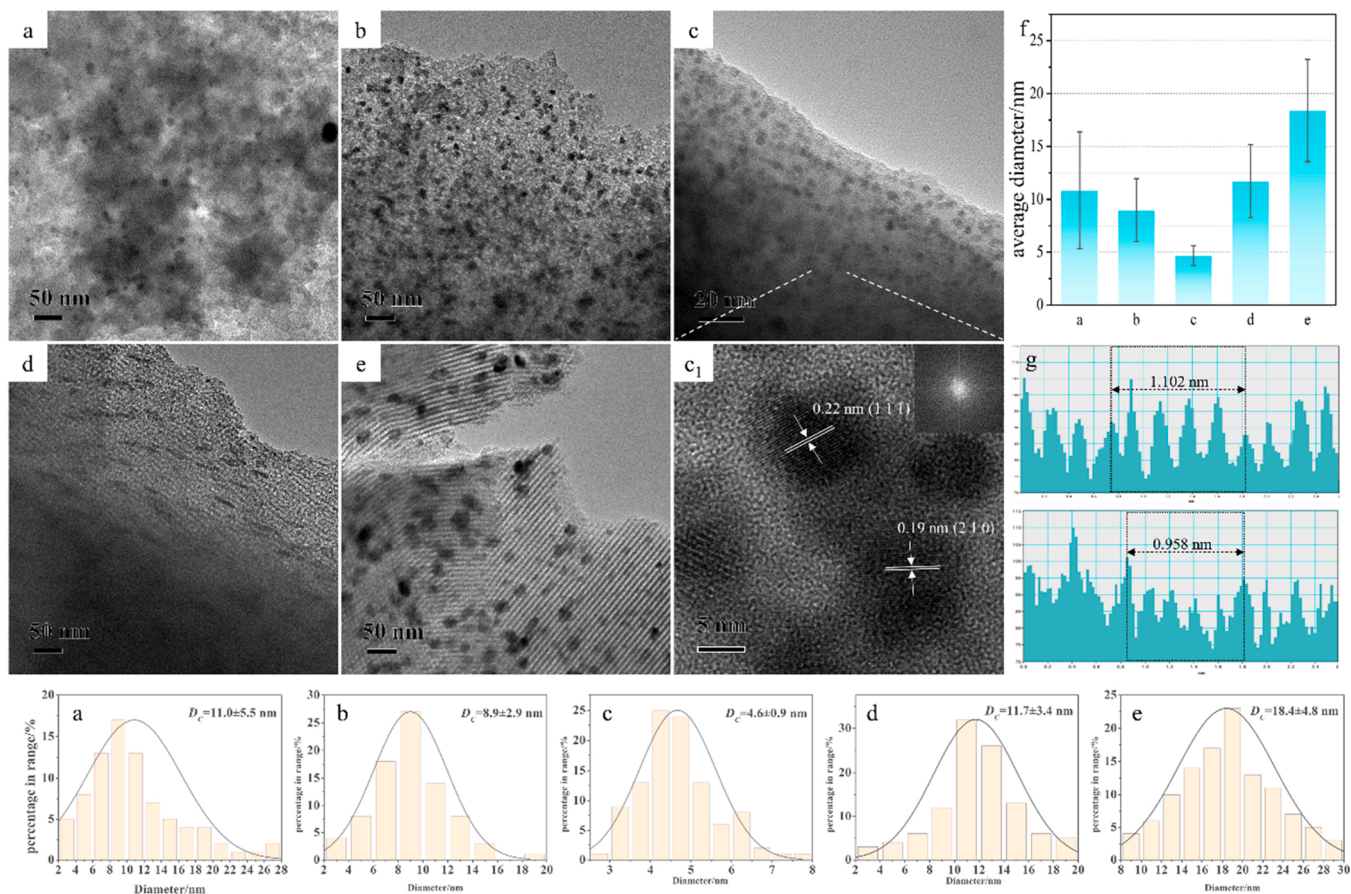


Fig. 7. TEM images and the Ni₂P particles size distributions of the series of catalysts: Ni₂P/H-beta (a), Ni₂P/H-beta@SBA-16-1 (b), Ni₂P/H-beta@SBA-16-2 (c), Ni₂P/H-beta@SBA-16-3 (d), Ni₂P/SBA-16 (e).

accompanying peak each.[55] Peaks with binding energies of 852.6–852.9 eV are assigned to the Ni^{δ+} ($0 < \delta < 1$) species in the Ni₂P crystals. Those at 856.4–857.3 eV are assigned to the Ni²⁺ species in the passivation layer on the surface of Ni₂P crystals interacting with P species. Other peaks, centered at the high binding energy side, are assigned to the Ni 2p_{1/2} signals. The peak with a binding energy of 129.5–129.6 eV is assigned to the P^{δ-} ($0 < \delta < 1$) species in the Ni₂P crystals while the peak at 134.2–134.8 eV is assigned to the P⁵⁺ species of PO₄³⁻ in the passivation layer on the surface of Ni₂P crystals. Here, all

the Ni₂P catalysts present Ni^{δ+} and P^{δ-} peaks at binding energies of 853.3 eV and 129.6 eV, and the peak intensity of Ni on Ni₂P/H-beta@SBA-16-2 is stronger than that of the other samples. The surface atomic ratios of the Ni₂P catalysts are displayed in Table 2. It shows that the P/Ni on the catalysts are all higher than the theoretical values (Ni₂P, 0.5), which indicates that more p species migrated to the surface of the catalysts during the formation of the Ni₂P phase. In addition, the P/Ni of the catalyst surface increases in the following sequence: Ni₂P/H-beta@SBA-16-2 (2.25) < Ni₂P/H-beta (2.75)

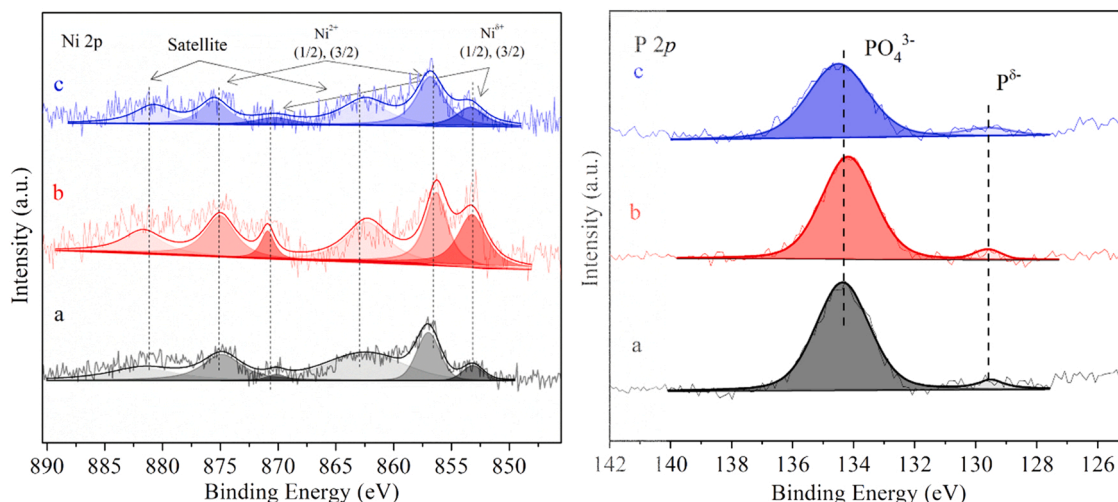


Fig. 8. XPS spectra of the series of catalysts: Ni₂P/H-beta (a), Ni₂P/H-beta@SBA-16-2 (b), Ni₂P/SBA-16 (c).

< Ni₂P/SBA-16 (2.86), indicating that less P element was packed on the surface of Ni₂P/H-beta@SBA-16-2. In addition, the Ni/ (Si + Al) on the surface of Ni₂P/H-beta@SBA-16-2 catalyst was higher than that of the other two samples (0.023 and 0.013), which indicates that the introduction of mesoporous shell layer was beneficial to form more Ni₂P phase on the external surface of the catalyst.

The H₂-TPR profiles further demonstrate that the core-shell support encourages Ni₂P phase development. In the formation of Ni₂P, PH₃ was disproportionately pyrolyzed out of NaH₂PO₄, and subsequently followed the gas flow to disperse onto the precursor to reduce Ni species to form Ni₂P [56,57]. As can be seen from Fig. 9, H₂ consumption appeared two main peaks with increasing reduction temperature. The hydrogen consumption peak at lower temperature corresponds to the reduction of Ni species and low valent P species, and the peak at higher temperature corresponds to the reduction of P species in other phosphates [37]. It is found that Ni₂P/H-beta catalyst exhibits the highest Ni species reduction temperature. The Ni species reduction temperature of catalyst Ni₂P/SBA-16 is significantly lower than the other two samples. This is due to the SBA-16 materials being significantly less acidic than the other samples and Ni species tend to combine more strongly with acidic hydroxyl groups on the support (Fig. 6). However, the reduction

temperature of Ni species by catalyst Ni₂P/H-beta@SBA-16-2 is in between, suggesting that the introduction of core-shell structure can effectively adjust the MSI. Moreover, the second hydrogen consumption peak temperature of the core-shell catalyst Ni₂P/H-beta@SBA-16-2 is lower than that of the other samples. This illustrates less accumulation of phosphate appeared on the Ni₂P/H-beta@SBA-16-2, which was also consistent with the results of XPS.

3.3. HDN catalytic activity

The HDN activity of Ni₂P catalysts was evaluated using quinoline as a model compound. From the trend in the results shown in Fig. 10, the HDN activity over the Ni₂P catalyst at 380 °C follows the order: Ni₂P/H-beta@SBA-16-2 > Ni₂P/H-beta@SBA-16-3 > Ni₂P/H-beta@SBA-16-1 > Ni₂P/H-beta > Ni₂P/SBA-16. The Ni₂P/H-beta@SBA-16-2 catalyst showed the highest HDN activity (81.6%) when the temperature was 400 °C, which was about 1.7 times that of Ni₂P/SBA-16 (46.1%). In addition, Ni₂P/H-beta, Ni₂P/H-beta@SBA-16-1 and Ni₂P/H-beta@SBA-16-3 catalysts exhibited close or slightly lower activities in the range 340–380 °C, due to their similar Ni₂P particle size and in turn similar

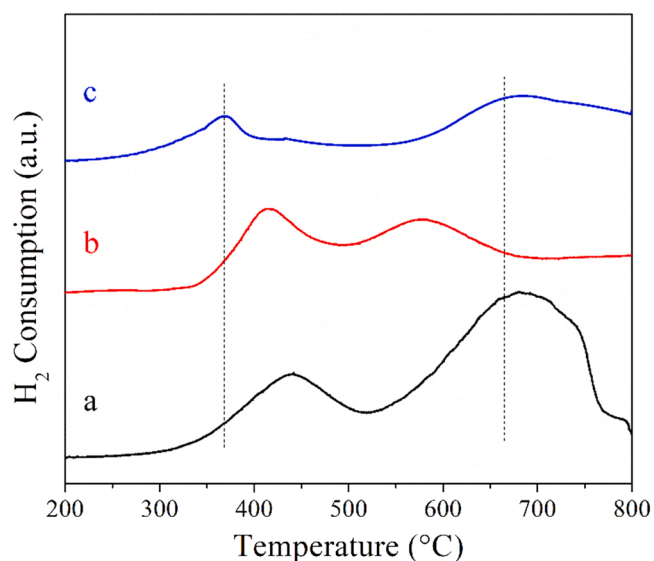


Fig. 9. H₂-TPR profiles of the calcined catalysts: Ni₂P/H-beta (a), Ni₂P/H-beta@SBA-16-2 (b), Ni₂P/SBA-16 (c).

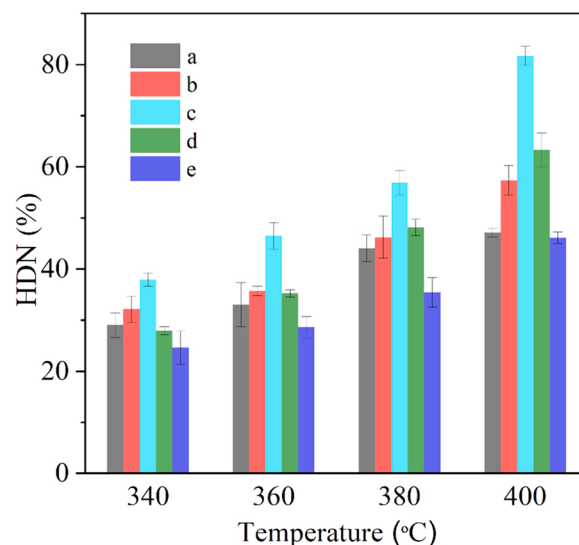


Fig. 10. HDN activity of the series of catalysts: Ni₂P/H-beta (a), Ni₂P/H-beta@SBA-16-1 (b), Ni₂P/H-beta@SBA-16-2 (c), Ni₂P/H-beta@SBA-16-3 (d), Ni₂P/SBA-16 (e).

numbers of active sites. When the reaction was continued by increasing the temperature to 400 °C, the activity of Ni₂P/H-beta was significantly lower than that of the other two samples. This is mainly because H-Beta is a pure microporous material with more acidic sites, so carbon accumulation is more likely to occur on the catalyst during reaction leading to pore blockage and a decrease in the contact of reactants with active sites.

The reaction products of quinoline hydrogenation were further analyzed by GC-MS. A summary of the results is shown in Fig. 11. It can be seen that there are two reaction routes for the hydrogenation of quinoline: the ring opening route Q→THQ1→OPA→PB and the hydrogenation saturation route Q→DHQ→PCHA→PCH + PCHE [44]. Hence, the proportion of the component contents of PCH + PCHE and PB could represent which reaction path the reaction tended to be. Table 4 presents the product distribution for HDN results over different catalysts. From Table 4, it can be seen that the (PCH + PCHE)/PB of Ni₂P/H-beta and series core-shell catalysts containing microporous zeolite are significantly higher than that of Ni₂P/SBA-16. This may be due to the catalyst containing microporous zeolites having smaller nickel phosphide particle size while containing a large number of small Ni₂P clusters anchored to the microporous channels of zeolites. Furthermore, since Ni₂P/H-beta@SBA-16-2 has more active centers for hydrogenation, it increases HDN activity from the hydrogenation saturation pathway.

The intrinsic HDN catalytic activity of Ni₂P catalyst is compared by k_{HDN} and TOF values. As shown in Table 5, Ni₂P/H-beta@SBA-16-2 catalyst shows both the highest reaction rate constant and TOF compared with other catalysts, with a k_{HDN} value about 2 times that of Ni₂P/SBA-16.

4. Discussion

The Ni₂P/H-beta@SBA-16-2 catalyst with a suitable thickness shell layer exhibited the highest HDN activity compared to other nickel phosphide catalysts. This can be explained as follows.

Firstly, the mechanism of core-shell structure formation with zeolites as core oxides as shells is proposed. During the formation of core-shell structure, silicon sources generate through three-dimensional worm-like mesopores on H-Beta zeolite surface by electrostatic adsorption deposition. This is followed by the formation of ordered mesoporous SBA-16 shell under the guidance of F127 (Fig. 2c, d). This can be demonstrated from TEM images that when the silicon source content is low, the silicon source preferentially grows a layer of worm like mesopores on the surface of zeolites (Fig. 2b). The shell layer is more easily coated on the edge of the zeolite core, and the smoother the surface of the core, the more uniform the thickness of the shell layer (Fig. S9). Two other core-shell materials were prepared with increasing silicon source

content but without hydrothermal crystallization (Fig. S2), and the silicon source continued irregularly growing disordered worm like mesoporous structures on the zeolite surface. This point can be further demonstrated from the pore size distribution (Fig. 1D). It can be seen that in addition to having one peak centered at 4 nm, the core-shell structured materials present a broad distribution of mesopores ranging from 5 to 15 nm. The formation process of the core-shell structure is shown in Scheme 1. It is important to note that a single idealized cubic model is used for convenience in this paper.

Secondly, the introduction of mesoporous shell can effectively improve the porosity, pore volume and specific surface area of catalysts (Table 1), which can provide enough space for HDN reaction and promote the movement of reactants and products. SBA-16 has three-dimensional cubic pore channel mesopores and is connected to H-Beta zeolites through three-dimensional worm like mesopores at the interface, making the pore channels continuous throughout the core-shell structure. This promotes free movement of reactive molecules throughout the material. In addition, the thicker shell layer would affect the accessibility between Ni₂P metal and reactant molecules, increasing the diffusion resistance of reactants on the catalyst surface. The open pore structure enhances contact of reactant molecules with Ni₂P active sites and lower carbon accumulation (that leads to pore clogging) occurs at the catalyst surface, evident from the HDN results (Fig. 10). The microporous zeolite catalysts exhibited similar catalytic activities with Ni₂P/H-beta@SBA-16-1 and Ni₂P/H-beta@SBA-16-3 in the range of 340–380 °C, while the activity of Ni₂P/H-beta at 400 °C was significantly lower than the other two core-shell catalysts when the reaction continued.

Thirdly, a core-shell structure of suitable thickness is beneficial for the formation of Ni₂P catalysts with more uniform and smaller average particle size. The H-Beta zeolite core can provide abundant acidic sites, and its microporous pore structure can anchor Ni and P species that enter into the pore channels, which is beneficial for the formation of many tiny (1–2 nm) nanoclusters (Fig. S3). Furthermore, during the reduction of catalysts, Ni species inside the zeolite pore migrate to the material surface to form Ni₂P phase [37,58]. In this process, the higher external surface area of the material favors to provide enough space for Ni and P species to migrate to form a highly dispersed Ni₂P phase. Here, a smaller particle size Ni₂P phase could be observed for Ni₂P/H-Beta, but its particle size distribution was significantly wider than that of the other samples (Fig. 7). This is due to the agglomeration of Ni and P species in the process of migrating to form Ni₂P. Larger Ni₂P particles (> 20 nm) are observed from TEM images. Moreover, it has been well reported that improved the acidity of a weakly acidic material (MCM-41) results in a catalyst that exhibits smaller Ni₂P particles and higher active phase dispersions [34]. In this paper, the B/L ratio of the support can be

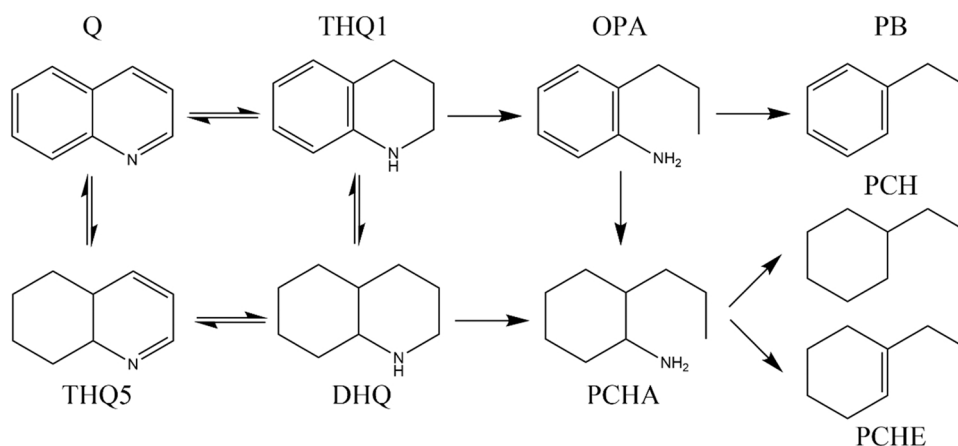


Fig. 11. HDN reaction network of quinoline. Q: quinoline; THQ5: 5,6,7,8-tetrahydroquinoline; DHQ: decahydroquinoline; THQ1: 1,2,3,4-tetrahydroquinoline; OPA: ortho-propylaniline; PCHA: 2-propylcyclohexylamine; PCHE: propylcyclohexene; PCH: propylcyclohexane; PB: propylbenzene.

Table 4Product selectivities of the Ni₂P catalysts in the HDN reaction at 380 °C.

Catalysts	Product selectivity (%)					
	PCH+PCHE	PB	DHQ	THQ5 +THQ1	OPA	(PCH+PCHE)/PB
Ni ₂ P/H-beta	43.7	10.8	8.6	31.3	5.6	4.05
Ni ₂ P/H-beta@SBA-16-1	42.2	9.9	8.8	32.5	6.6	4.26
Ni ₂ P/H-beta@SBA-16-2	54.6	9.7	7.9	19.5	8.3	5.63
Ni ₂ P/H-beta@SBA-16-3	41.5	10.4	9.1	29.8	9.2	3.99
Ni ₂ P/SBA-16	28.2	14.6	8.4	32.5	16.3	1.93

Table 5Intrinsic activities of the Ni₂P catalysts in the HDN of quinoline.^a

Catalysts	k_{HDN} (10^{-2} $\mu\text{mol g}^{-1} \text{s}^{-1}$)	TOF (10^{-3}s^{-1})
Ni ₂ P/H-beta	7.31	1.2
Ni ₂ P/H-beta@SBA-16-1	8.88	1.2
Ni ₂ P/H-beta@SBA-16-2	14.22	1.7
Ni ₂ P/H-beta@SBA-16-3	9.01	1.4
Ni ₂ P/SBA-16	6.97	1.1

^a Reaction conditions: $T = 380$ °C, $P = 4.0$ MPa, H_2 flow rate 60 mL min^{-1} , quinoline molar feed rate $0.107 \mu\text{mol s}^{-1}$.

adjusted by changing the thickness of the shell layer, and Ni species can easily combine with the abundant acidic hydroxyl groups of the support to generate a smaller particle size active phase. From the H₂-TPR results, it can be seen that the introduction of core-shell structure can also adjust the MSI of the materials, reduce the aggregation of Ni species in the reduction, and improve the dispersity of the active phase.

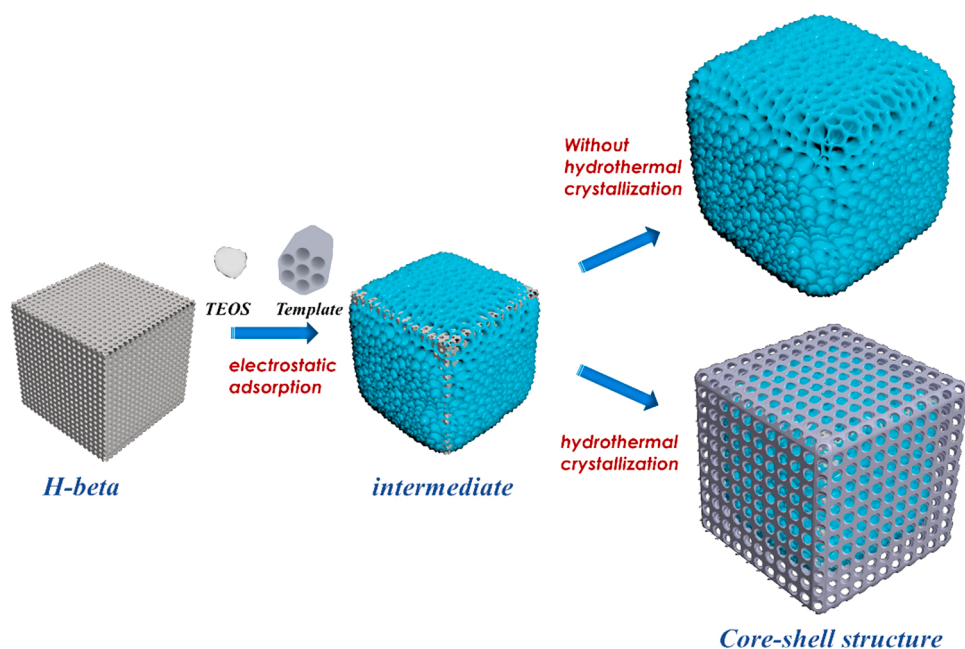
Furthermore, the core-shell catalyst with a smaller particle size of Ni₂P contains more Ni (2) active phase, resulting in the catalyst having more active centers for hydrogenation. It is widely reported that the bond energy of the C=N bond (615 kJ/mol) is much higher than that of the C-N bond (305 kJ/mol) [59]. So for quinoline, first hydrogenation followed by denitrification would make the reaction activation energy lower and more favorable for the reaction to proceed. From the reaction product results, the catalyst increased HDN activity through the hydrogenation saturation path and exhibited the highest TOF. Moreover, the carbon nitrogen bond breaking process is a key step in the HDN reaction, and the B acid content similarly affects the carbon nitrogen

bond breaking. Nelson et al. [49] reported the Hofmann elimination mechanism (E₂) and argues that the B acid can protonate the N to form a readily separable quaternary amine group, which subsequently occurs β -Elimination to form alkenes. Therefore, the B acid site is an important active site in the deamination of the N atom. In this paper, the B/L ratio of the supports can be adjusted by changing the shell thickness. The Ni₂P/H-beta@SBA-16-2 catalyst has a higher amount of B acid, while the B/L ratio of Ni₂P/H-beta@SBA-16-3 with a higher shell thickness shows an obvious decrease.

In summary, the Ni₂P/H-beta@SBA-16-2 catalyst shows higher k_{HDN} and TOF which can be attributed to its smaller particle size and homogeneous Ni₂P phase, moderate shell thickness, open channel structure, larger surface and external surface area, large pore volume, appropriate MSI and moderate B/L ratio.

5. Conclusion

In this paper, a series of Ni₂P/H-beta@SBA-16-x core-shell catalysts with tunable shell thickness were controllably synthesized for the HDN of quinolines. A core-shell structure formation mechanism with zeolites as core oxides as shells is proposed. Silicon sources first deposit on the surface of zeolites by electrostatic adsorption forming irregular pore channels, followed by the growth of ordered shells under the action of templates. The introduction of core-shell structures can effectively adjust the MSI of materials. The higher external surface area provided by the unique core-shell structure makes the Ni species and P species highly dispersed during the formation of Ni₂P phase, which is favorable to the formation of Ni₂P nanoparticles with uniform particle size. The introduction of mesoporous shells with different thickness can be used to

**Scheme 1.** The formation process of core-shell structure.

adjust the acidity as well as the ratio of B/L acid sites, which is beneficial for the formation of Ni₂P phase with smaller average particle size. Moreover, the mesoporous shell layer provides a higher pore volume and open pore structure, which promotes contact between reactant molecules and active sites during hydrogenation and reduces carbon accumulation. Consequently, the Ni₂P/H-beta@SBA-16-2 catalyst demonstrated the best HDN activity and TOF. Moreover, the hydrogenation saturation route was the prior route for HDN of quinoline on Ni₂P/H-beta@SBA-16-2 catalyst due to its higher B acid content and more Ni (2) active sites arising from smaller nickel phosphide particles, which significantly enhanced the HDN activity.

CRedit authorship contribution statement

Hanzhang Gong: Conceptualization, Writing – original draft preparation, Investigation. **Yuan Zhuang:** Data curation, Resources, Investigation. **Xiao Zhang:** Writing – review & editing, Visualization. **Jian Liu:** Supervision, Writing – review & editing. **Shuyuan Li:** Project administration.

Declaration of Competing Interest

The authors declare that they have no known competing financial interests or personal relationships that could have appeared to influence the work reported in this paper.

Data Availability

Data will be made available on request.

Acknowledgments

This work was supported by Shanxi Provincial Key Research and Development Project (No. 20201102002), National Key Research and Development Program of China (2019YFC1907602) and National Natural Science Key Foundation of China (22035009).

Appendix A. Supporting information

Supplementary data associated with this article can be found in the online version at [doi:10.1016/j.apcatb.2023.122574](https://doi.org/10.1016/j.apcatb.2023.122574).

References

- [1] W. Chen, F. Maugé, J. van Gestel, H. Nie, D. Li, X. Long, Effect of modification of the alumina acidity on the properties of supported Mo and CoMo sulfide catalysts, *J. Catal.* 304 (2013) 47–62.
- [2] M. Bachrach, T.J. Marks, J.M. Notestein, Understanding the hydrodenitrogenation of heteroaromatics on a molecular level, *ACS Catal.* 6 (2016) 1455–1476.
- [3] W. Huang, Y. Zhou, Q. Wei, X. Liu, P. Zhang, Z. Xu, Z. Yu, X. Wang, H. Liu, X. Dai, H. Yang, Synthesis of mesoporous TiO₂-Al₂O₃ composites supported NiW hydrotreating catalysts and their superior catalytic performance for heavy oil hydrodenitrogenation, *Fuel* 319 (2022).
- [4] Y. Yin, W. Chen, G. Wu, F. Xin, K. Qin, Y. Lu, L. Zhang, M. Li, Kinetics toward mechanism and real operation for ultra-deep hydrodesulfurization and hydrodenitrogenation of diesel, *AIChE J.* 67 (2021).
- [5] M. Karimi Boroujeni, A. Irankhah, Performance study of Ni, Co, and Mo catalysts supported on γ -Al₂O₃ and HZSM5 in HDS reactions of mixed naphtha, *Int. J. Energy Res.* 46 (2021) 995–1007.
- [6] Y. Guo, H. He, X. Liu, Z. Chen, R.M. Rioux, M.J. Janik, P.E. Savage, Ring-opening and hydrodenitrogenation of indole under hydrothermal conditions over Ni, Pt, Ru, and Ni-Ru bimetallic catalysts, *Chem. Eng. J.* 406 (2021).
- [7] F.A. Braggio, M.D. Mello, B.C. Magalhães, J.L. Zotin, M.A.P. Silva, Effect of pH on activity of NiMo/Al₂O₃ catalysts prepared with citric acid in simultaneous hydrodesulfurization and hydrodenitrogenation reactions, *Catal. Lett.* 147 (2017) 1104–1113.
- [8] V. Sundaramurthy, A. Dalai, J. Adjaye, HDN and HDS of different gas oils derived from Athabasca bitumen over phosphorus-doped NiMo/ γ -Al₂O₃ carbides, *Appl. Catal. B* 68 (2006) 38–48.
- [9] B. Behnejad, M. Abdouss, A. Tavasoli, Comparison of performance of Ni–Mo/ γ -alumina catalyst in HDS and HDN reactions of main distillate fractions, *Pet. Sci.* 16 (2019) 645–656.
- [10] X. Liu, X. Li, Z. Yan, Facile route to prepare bimodal mesoporous γ -Al₂O₃ as support for highly active CoMo-based hydrodesulfurization catalyst, *Appl. Catal. B* 121–122 (2012) 50–56.
- [11] T. Zhu, H. Song, X. Dai, H. Song, Preparation of Ni₂P/Al-SBA-15 catalyst and its performance for benzofuran hydrodeoxygenation, *Chin. J. Chem. Eng.* 25 (2017) 1784–1790.
- [12] X. Zhu, L.L. Lobban, R.G. Mallinson, D.E. Resasco, Bifunctional transalkylation and hydrodeoxygenation of anisole over a Pt/HBeta catalyst, *J. Catal.* 281 (2011) 21–29.
- [13] R. Martínez Guerrero, A. Hernández-Gordillo, V. Santes, J.R. Vargas García, J. Escobar, L. Díaz-García, L. Díaz Barriga Arceo, V. Garibay Febles, Monometallic Pd and Pt and Bimetallic Pd-Pt/Al₂O₃-TiO₂ for the HDS of DBT: Effect of the Pd and Pt incorporation method, *J. Chem.* 2014 (2014) 1–10.
- [14] T. Tang, C. Yin, L. Wang, Y. Ji, F. Xiao, Good sulfur tolerance of a mesoporous Beta zeolite-supported palladium catalyst in the deep hydrogenation of aromatics, *J. Catal.* 257 (2008) 125–133.
- [15] F. Jiao, H. Guo, Y. Chai, H. Awala, S. Mintova, C. Liu, Synergy between a sulfur-tolerant Pt/Al₂O₃@sodalite core-shell catalyst and a CoMo/Al₂O₃ catalyst, *J. Catal.* 368 (2018) 89–97.
- [16] S.T. Oyama, Novel catalysts for advanced hydroprocessing: transition metal phosphides, *J. Catal.* 216 (2003) 343–352.
- [17] M. Dorneles de Mello, F. de Almeida Braggio, B. da Costa Magalhães, J.L. Zotin, M. A.P. da Silva, Effects of phosphorus content on simultaneous ultradeep HDS and HDN reactions over NiMoP/Alumina catalysts, *Ind. Eng. Chem. Res.* 56 (2017) 10287–10299.
- [18] A.I. d'Aquino, S.J. Danforth, T.R. Clinkingbeard, B. Ilıc, L. Pullan, M.A. Reynolds, B.D. Murray, M.E. Bussell, Highly-active nickel phosphide hydrotreating catalysts prepared in situ using nickel hypophosphite precursors, *J. Catal.* 335 (2016) 204–214.
- [19] M. Peroni, G. Mancino, E. Baráth, O.Y. Gutiérrez, J.A. Lercher, Bulk and γ -Al₂O₃-supported Ni₂P and MoP for hydrodeoxygenation of palmitic acid, *Appl. Catal. B* 180 (2016) 301–311.
- [20] J.A. Cecilia, A. Infantes-Molina, E. Rodríguez-Castellón, A. Jiménez-López, Dibenzothiophene hydrodesulfurization over cobalt phosphide catalysts prepared through a new synthetic approach: effect of the support, *Appl. Catal. B* 92 (2009) 100–113.
- [21] M. Shao, H. Cui, S. Guo, L. Zhao, Y. Tan, Effects of calcination and reduction temperature on the properties of Ni-P/SiO₂ and Ni-P/Al₂O₃ and their hydrodenitrogenation performance, *RSC Adv.* 8 (2018) 6745–6751.
- [22] S. Oyama, Y. Lee, The active site of nickel phosphide catalysts for the hydrodesulfurization of 4,6-DMDBT, *J. Catal.* 258 (2008) 393–400.
- [23] Y. Shu, Y. Lee, S. Oyama, Structure-sensitivity of hydrodesulfurization of 4,6-dimethyldibenzothiophene over silica-supported nickel phosphide catalysts, *J. Catal.* 236 (2005) 112–121.
- [24] D. Liu, A. Wang, C. Liu, R. Prins, Bulk and Al₂O₃-supported Ni₂P HDS catalysts prepared by separating the nickel and hypophosphite sources, *Catal. Commun.* 77 (2016) 13–17.
- [25] T. Chen, B. Yang, S. Li, K. Wang, X. Jiang, Y. Zhang, G. He, Ni₂P catalysts supported on titania-modified alumina for the hydrodesulfurization of dibenzothiophene, *Ind. Eng. Chem. Res.* 50 (2011) 11043–11048.
- [26] X. Wang, C. Xiao, J. Mei, M.H. Alabsi, Y. Shi, Z. Zhao, A. Duan, K.W. Huang, C. Xu, Structural screening and design of dendritic micro-mesoporous composites for efficient hydrodesulfurization of dibenzothiophene and 4,6-Dimethyldibenzothiophene, *ACS Appl. Mater. Interfaces* 12 (2020) 40404–40414.
- [27] O.Y. Gutiérrez, S. Singh, E. Schachtl, J. Kim, E. Kondratieva, J. Hein, J.A. Lercher, Effects of the Support on the performance and promotion of (Ni)MoS₂ catalysts for simultaneous hydrodenitrogenation and hydrodesulfurization, *ACS Catal.* 4 (2014) 1487–1499.
- [28] C.A. Badari, F. Lónyi, E. Drotár, A. Kaszonyi, J. Vályon, A study of the hydrodenitrogenation of propylamine over supported nickel phosphide catalysts using amorphous and nanostructured silica supports, *Appl. Catal. B* 164 (2015) 48–60.
- [29] Q. Guan, W. Li, M. Zhang, K. Tao, Alternative synthesis of bulk and supported nickel phosphide from the thermal decomposition of hypophosphites, *J. Catal.* 263 (2009) 1–3.
- [30] J.-G. Jang, Y.-K. Lee, Promotional effect of Ga for Ni₂P catalyst on hydrodesulfurization of 4,6-DMDBT, *Appl. Catal. B* 250 (2019) 181–188.
- [31] Y.-K. Lee, S.T. Oyama, Sulfur resistant nature of Ni₂P catalyst in deep hydrodesulfurization, *Appl. Catal. A* 548 (2017) 103–113.
- [32] G.-N. Yun, K.-D. Kim, Y.-K. Lee, Hydrotreating of waste tire pyrolysis oil over highly dispersed Ni₂P catalyst supported on SBA-15, *Catalysts* 11 (2021).
- [33] P.J. Topalian, D.R. Liyanage, S.J. Danforth, A.I. d'Aquino, S.L. Brock, M.E. Bussell, Effect of particle size on the deep HDS properties of Ni₂P catalysts, *J. Phys. Chem. C* 123 (2019) 25701–25711.
- [34] H. Song, J. Wang, Z. Wang, H. Song, F. Li, Z. Jin, Effect of titanium content on dibenzothiophene HDS performance over Ni₂P/Ti-MCM-41 catalyst, *J. Catal.* 311 (2014) 257–265.
- [35] J. Zhu, R. Osuga, R. Ishikawa, N. Shibata, Y. Ikubara, J.N. Kondo, M. Ogura, J. Yu, T. Wakihara, Z. Liu, T. Okubo, Ultrafast encapsulation of metal nanoclusters into MFI zeolite in the course of its crystallization: catalytic application for propane dehydrogenation, *Angew. Chem. Int. Ed. Engl.* (2020).
- [36] R.J. White, A. Fischer, C. Goebel, A. Thomas, A. Sustainable, Template for mesoporous zeolite synthesis, *J. Am. Chem. Soc.* 136 (2014) 2715–2718.
- [37] L. Zhang, W. Fu, Q. Yu, T. Tang, Y. Zhao, H. Zhao, Y. Li, Ni₂P clusters on zeolite nanosheet assemblies with high activity and good stability in the

- hydrodesulfurization of 4,6-dimethyldibenzothiophene, *J. Catal.* 338 (2016) 210–221.
- [38] W. Zhou, M. Liu, Q. Zhang, Q. Wei, S. Ding, Y. Zhou, Synthesis of NiMo catalysts supported on gallium-containing mesoporous γ zeolites with different gallium contents and their high activities in the hydrodesulfurization of 4,6-Dimethyldibenzothiophene, *ACS Catal.* 7 (2017) 7665–7679.
- [39] H.J. Cho, D. Kim, J. Li, D. Su, B. Xu, Zeolite-Encapsulated Pt nanoparticles for tandem catalysis, *J. Am. Chem. Soc.* 140 (2018) 13514–13520.
- [40] L. Zhang, W. Fu, Q. Yu, T. Tang, Y. Zhao, Y. Li, Effect of citric acid addition on the morphology and activity of Ni_2P supported on mesoporous zeolite ZSM-5 for the hydrogenation of 4,6-DMDBT and phenanthrene, *J. Catal.* 345 (2017) 295–307.
- [41] W. Fu, L. Zhang, D. Wu, Q. Yu, T. Tang, T. Tang, Mesoporous zeolite ZSM-5 supported Ni_2P catalysts with high activity in the hydrogenation of phenanthrene and 4,6-Dimethyldibenzothiophene, *Ind. Eng. Chem. Res.* 55 (2016) 7085–7095.
- [42] Q. Huo, Y. Gong, T. Dou, Z. Zhao, H. Pan, F. Deng, Novel micro- and mesoporous composite molecular sieve assembled by Zeolite L nanocrystal and its performance for the hydrodesulfurization (HDS) of Fluid Catalytic Cracking (FCC) gasoline†, *Energy Fuels* 24 (2010) 3764–3771.
- [43] Y. Wang, J. Song, N.C. Baxter, G.-T. Kuo, S. Wang, Synthesis of hierarchical ZSM-5 zeolites by solid-state crystallization and their catalytic properties, *J. Catal.* 349 (2017) 53–65.
- [44] Q. Meng, A. Duan, C. Xu, Z. Zhao, J. Li, B. Wang, C. Liu, D. Hu, H. Li, Y. Li, Synthesis of novel hierarchically porous NiMo/ZSM-5-KIT-5 catalysts and their superior performance in hydrodenitrogenation of quinoline, *Catal. Sci. Technol.* 8 (2018) 5062–5072.
- [45] J. Xu, Y. Guo, T. Huang, Y. Fan, Decamethonium bromide-dispersed palladium nanoparticles on mesoporous HZSM-5 zeolites for deep hydrodesulfurization, *Chem. Eng. J.* 333 (2018) 206–215.
- [46] J.-L. Mei, Y. Shi, C.-K. Xiao, A.-C. Wang, A.-J. Duan, X.-L. Wang, Hierarchically porous Beta/SBA-16 with different silica-alumina ratios and the hydrodesulfurization performances of DBT and 4,6-DMDBT, *Pet. Sci.* 19 (2022) 375–386.
- [47] Q. Meng, A. Wang, C. Liu, E. Wang, A. Duan, Z. Zhao, G. Jiang, Preparation of Beta-KIT-5 composite material supported ternary metal catalyst and its hydrodenitrogenation performance of quinoline, *Fuel* 326 (2022).
- [48] G. Yun, Q. Guan, W. Li, Nondestructive construction of Lewis acid sites on the surface of supported nickel phosphide catalysts by atomic-layer deposition, *J. Catal.* 361 (2018) 12–22.
- [49] N. Nelson, R.B. Levy, The organic chemistry of hydrodenitrogenation, *J. Catal.* 58 (1979) 485–488.
- [50] H. Wu, A. Duan, Z. Zhao, T. Li, R. Prins, X. Zhou, Synthesis of NiMo hydrodesulfurization catalyst supported on a composite of nano-sized ZSM-5 zeolite enwrapped with mesoporous KIT-6 material and its high isomerization selectivity, *J. Catal.* 317 (2014) 303–317.
- [51] H. Sun, Q. Wang, X. Zhang, Q. Yu, L. Li, Y. Wang, B. Shen, Hydrodesulfurization of dibenzothiophene over $\text{NiW}/(\text{SnAlPO}_4\text{-5}+\text{Al}_2\text{O}_3)$ catalyst, the tuning effect of $\text{SnAlPO}_4\text{-5}$ to the desulfurization reaction pathway, *Appl. Catal. A* 563 (2018) 137–145.
- [52] Y. Ganjkanlou, E. Groppo, S. Bordiga, M.A. Volkova, G. Berlier, Incorporation of Ni into HZSM-5 zeolites: Effects of zeolite morphology and incorporation procedure, *Microporous Mesoporous Mater.* 229 (2016) 76–82.
- [53] M.M. Mohamed, Structural and acidic characteristics of Cu-Ni-modified acid-leached mordenites, *J. Colloid Interface Sci.* 265 (2003) 106–114.
- [54] S. Kweon, J. Bae, Y. Cho, S. Lee, J. Kim, D. Jo, C.-H. Shin, M.B. Park, H.-K. Min, Defect-stabilized nickel on beta zeolite as a promising catalyst for dry reforming of methane, *Catal. Sci. Technol.* 12 (2022) 3106–3115.
- [55] X. Duan, X. Li, A. Wang, Y. Teng, Y. Wang, Y. Hu, Effect of TiO_2 on hydrodenitrogenation performances of MCM-41 supported molybdenum phosphides, *Catal. Today* 149 (2010) 11–18.
- [56] X. Lan, E.J.M. Hensen, T. Weber, Silica-supported Ni 2 P: effect of preparation conditions on structure and catalytic performance in thiophene hydrodesulfurization (HDS), *Catal. Today* 292 (2017) 121–132.
- [57] D. Liu, X. Li, L. Wei, T. Zhang, A. Wang, C. Liu, R. Prins, Disproportionation of hypophosphite and phosphite, *Dalton Trans.* 46 (2017) 6366–6378.
- [58] H. Gong, Z. Xiao, Y. Zhuang, S. Liang, X. Li, W. Zheng, A. Duan, X. Zhang, J. Liu, Core-shell meso-beta@mesoporous aluminosilicate supported Ni_2P catalyst for the hydrodenitrogenation of quinoline: effect of core shell structure on Ni_2P particle size, *Fuel* 302 (2021).
- [59] J. Kaur, B. Pal, Photocatalytic degradation of N-heterocyclic aromatics-effects of number and position of nitrogen atoms in the ring, *Environ. Sci. Pollut. Res. Int.* 20 (2013) 3956–3964.